Retrieval of geophysical parameters from Moderate Resolution Imaging Spectroradiometer thermal infrared data: evaluation of a two-step physical algorithm

Xia L. Ma, Zhengming Wan, Christopher C. Moeller, W. Paul Menzel, Liam E. Gumley, and Yulin Zhang

A two-step physical algorithm that simultaneously retrieves geophysical parameters from Moderate Resolution Imaging Spectroradiometer (MODIS) measurements was developed. The retrieved geophysical parameters include atmospheric temperature–humidity profile, surface skin temperature, and two surface emissivities within the shortwave (3–5-μm) and the longwave (8–14.5-μm) regions. The physical retrieval is accomplished in two steps: (i) The Tikhonov regularization method is employed to generate a regularization solution along with an optimum regularization parameter; (ii) the nonlinear Newtonian iteration algorithm is carried out with the regularization solution as a first-guess profile to obtain a final maximum probability solution for geophysical parameters. The algorithm was tested with both simulated and real MODIS Airborne Simulator (MAS) data. Sensitivity studies on simulated MAS data demonstrate that simultaneous retrievals of land and atmospheric parameters improve the accuracy of the retrieved geophysical parameters. Finally, analysis and accuracy of retrievals from real MAS data are discussed. © 2000 Optical Society of America

OCIS codes: 280.0280, 030.5620.

1. Introduction

The Moderate Resolution Imaging Spectroradiometer (MODIS)[1] is a keystone instrument of the Earth Observing System (EOS) for global remote sensing of atmosphere, land, and ocean properties from space in the visible and the infrared regions of the spectrum. It was developed as part of the EOS AM-1 platform (launched in December 1999) for global remote sensing of geophysical parameters from space. MODIS is a scanning spectroradiometer with 36 spectral bands between 0.41 and 14.5 μm. It scans from nadir to ±55°, with bands 1–19 and band 26 in the visible and the near-infrared range and with the remaining bands in the thermal infrared from the 3–14.5-μm spectral region. Although MODIS is not a sounding instrument, these thermal infrared bands provide measurements of radiance from the Earth's surface, from clouds, and from atmospheric carbon dioxide (CO_2), moisture (H_2O), and ozone (O_3). Thus it will be possible to retrieve geophysical parameters that include atmospheric temperature and water-vapor profiles, surface skin temperature, and land surface emissivities (henceforth abbreviated as surface emissivity) from the MODIS measurements. The combination of spectral coverage, high spatial resolution (1 km at nadir), and good radiometric signal to noise make MODIS particularly capable of retrieving medium-scale variability. In support of MODIS remote-sensing algorithm development the MODIS Airborne Simulator (MAS) was developed. MAS has 50 spectral bands with spectral coverage from 0.47 to 14.17 μm. Of the 50 MAS bands, 19 have corresponding bands on MODIS. With its much higher spectral resolution (50 m versus 250–

X. L. Ma (xma@icess.ucsb.edu), Z. Wan, and Y. Zhang are with the Institute for Computational Earth System Science, University of California, Santa Barbara, California, 93106. X. L. Ma, C. C. Moeller, and L. E. Gumley are with the Cooperative Institute for Meteorological Satellite Studies, University of Wisconsin-Madison, Madison, Wisconsin, 53706. W. P. Menzel is with the Office of Research and Applications, the National Oceanic and Atmospheric Administration, National Environmental Satellite Data Information Service, Madison, Wisconsin 53706.

Received 3 September 1999; revised manuscript received 28 April 2000.
0003-6935/00/203537-14$15.00/0
© 2000 Optical Society of America

Table 1. Spectral Characteristics of the MAS Sounding Bands in the 1996 Configuration

MAS Band	Equivalent MODIS Band	Central Wavelength (μm)	Spectral Resolution (μm)	NEΔT[a] (K)	Primary Use[b]
30		3.59	0.16	1.21	L
31	20	3.74	0.15	0.76	L, O
32	22	3.90	0.17	0.70	L
33	23	4.05	0.16	0.54	L
34		4.21	0.16	0.58	L
35		4.36	0.15	3.22	A
36	25	4.52	0.16	1.13	A
37		4.67	0.16	0.30	A
38		4.82	0.16	0.25	A
39		4.97	0.15	0.29	A
40		5.12	0.16	0.22	A
41		5.28	0.16	0.28	A
42	29	8.60	0.44	0.19	A, L
43	30	9.79	0.62	0.26	Ozone
44		10.55	0.49	0.11	A, L
45	31	11.02	0.54	0.13	A, L, O
46	32	11.96	0.45	0.23	A, L, O
47		12.88	0.46	0.39	A, L
48	33	13.23	0.47	0.50	A
49	35	13.72	0.60	1.27	A
50	36	14.17	0.42	2.63	A

[a]NEΔT for bands 30–50 are based on in-flight measurements over the Gulf of Mexico on 9 April 1996.
[b]A, atmospheric studies; L, land studies; O, ocean studies.

1000 m for MODIS), MAS is able to provide detailed small-scale variations of geophysical parameters[2] and assess the scientific capability and usefulness of MODIS bands. In the prelaunch phase a MODIS atmospheric retrieval algorithm was developed and tested with data from MAS.[2,3] MAS, flown on NASA's ER-2 high-altitude (20-km) research aircraft, contains spectral sounding bands that will be used in the evaluation of a two-step physical retrieval algorithm presented in this paper. Spectral characteristics of these bands and corresponding MODIS bands are listed in Table 1. Figure 1 shows the spectral responses of MAS infrared bands superposed with an emission spectrum from the surface and the atmosphere computed with a line-by-line radiative transfer model (LBLRTM)[4] for the U.S. standard atmosphere.

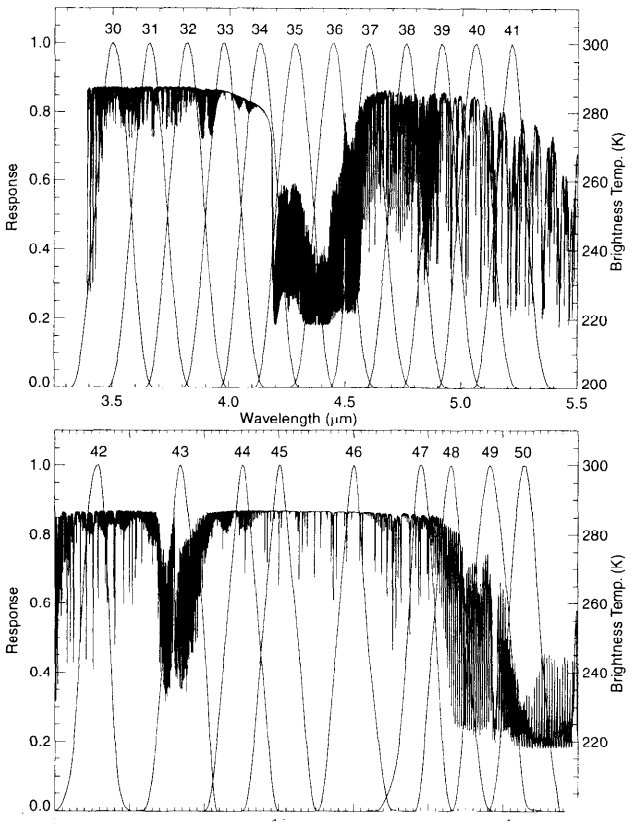

Remote sensing of atmospheric temperature and water-vapor profiles from infrared emission bands usually requires assumptions about the behavior of terrestrial materials. It is usually assumed that the surface is a blackbody (emissivity 1.0)[5–10] or a graybody (approximately 0.96–0.98)[11] for atmospheric sounding. In the current Geostationary Operational Environmental Satellite (GOES) operational retrieval algorithm a sequential method is used to deal with the surface emissivity. The sequential method first retrieves atmospheric parameters and surface skin temperature, using a constant surface emissivity of 0.96 for land or 0.98 for water[12]; then the surface emissivity is adjusted by use of the retrieved temperature–humidity profile and surface skin temperature in the radiative transfer equation (RTI

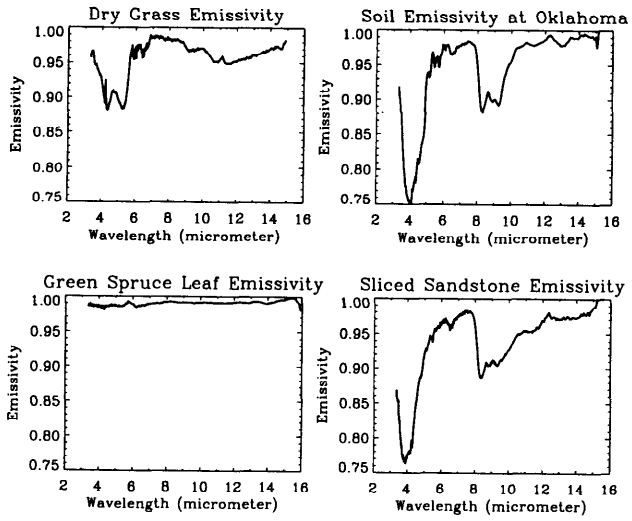

Fig. 2. Surface emissivity spectra in 3.5–14.5 μm for various terrestrial materials.

A drawback of this approach is that only a single surface emissivity within the longwave region is calculated, disregarding surface emissivity spectral variation. Moreover, sensitivity research on simulated MAS data has illustrated that separation of the surface emissivity retrieval from the atmospheric temperature–humidity profile retrieval in the coupled Earth–atmosphere system would reduce retrieval accuracy compared with that from the simultaneous retrieval. The surface emissivity is dependent on the surface composition (soil, vegetation, snow, wetness, and the like) and geometry (soil roughness, geometry of vegetation canopy, topography, and so on). For instance, large variations exist between vegetated and nonvegetated surfaces (e.g., rock, sand). Surface emissivity also varies within the shortwave (3–5-μm) and the longwave wave (8–14.5-μm) regions for some terrestrial materials. As shown in Fig. 2, the emissivity spectrum of a green spruce leaf is roughly constant from 3.5–14.5 μm (lower left-hand panel), but the emissivity spectrum of sliced sandstone (lower right-hand panel) has a large spectral variation. Thus, in cases of spectral and spatial surface emissivity variation, accounting for this variation will improve the accuracy of re-

the surface property retrieval in the Earth–atmosphere system, the land-surface temperature (LST) retrieval requires accurate information of the atmospheric temperature and water-vapor distribution for the correction of atmospheric influences. Although the split-window technique, which corrects atmospheric influences based on differential absorption in adjacent thermal bands, is less sensitive to the uncertainties of atmospheric status, this technique requires knowledge of surface emissivity to better than 0.01 for retrieval of LST to an accuracy of 1 K.[14] Obviously it is difficult to meet this requirement for land covers with variable emissivities, especially in semiarid and arid areas. Also, a recently developed physics-based LST retrieval algorithm[15] has demonstrated that the accuracy of the LST retrieval depends largely on accurate atmospheric information. These efforts indicate that the accuracy of retrieved geophysical parameters from space may be improved on by (i) including surface emissivity as a part of the solution of the RTE and (ii) retrieving atmospheric parameters and surface properties simultaneously.

In this paper a two-step physical algorithm that retrieves atmospheric temperature and water-vapor profiles, surface skin temperature, and two surface emissivities (in shortwave and longwave) is investigated. The linear simultaneous form of RTE, which is the basis of the two-step physical algorithm, was originally developed by Smith *et al.*[5–8] and has been successfully applied to radiometric measurements from the Television and Infrared Observational Satellite (TIROS) Operational Vertical Sounder (TOVS), GOES, and high-resolution interferometer sounder (HIS).[9–11,16–18] For example, Huang[16] derived a linearized RTE with analytical Jacobians of band transmittances and used Tikhonov regularization with a special side constraint on simulated and observed high-resolution interferometer sounder data. Eyre[19,20] proposed a Newtonian iteration algorithm that performs a simultaneous retrieval of the temperature and humidity profiles, the surface skin temperature, microwave emissivity, and the cloud-top pressure and amount from the TOVS data. However, in these efforts, a constant surface emissivity value was assumed for the infrared shortwave and longwave regions. It is expected that retrieval errors are increased over nonvegetated surfaces by means of ignoring surface emissivity spectral and spatial variations. This is supported by the findings of Plokhenko and Menzel,[13] who point out that even small emissivity variations cause measurable changes in infrared radiance and that disregarding the spectral and spatial variations of the emissivity in the window bands magnifies the errors in the forward transfer model calculation. Smith *et al.*[21] developed a physical retrieval algorithm for the atmospheric infrared sounder (AIRS) in which surface emissivity is treated as a retrieval parameter. This study follows Smith's derivation and expands on the early GOES physical retrieval development by including surface emissivities as a part of the re-

The two-step physical retrieval described in this paper requires the use of initial temperature and water-vapor profiles, surface skin temperature, and two surface emissivities. These initial geophysical parameters serve as a first guess to constrain the numerical solution to a physically reasonable results. The first-guess parameters are obtained through a statistical regression analysis technique (see Subsection 6.A). Then the physical retrieval is accomplished in two steps: (i) The Tikhonov regularization method is employed to generate a regularization solution that updates the first-guess temperature and water-vapor profiles, surface skin temperature, and two emissivities. Along with the Tikhohov solution, the optimum

of the Tikhonov regularization parameter that balances the residual norm and the side constraint norm (see Subsection 2.C) in the computed solution is also obtained. (ii) The Tikhonov regularization solution with the optimum regularization parameter is then used as an improved first guess in the nonlinear Newtonian iteration algorithm. The maximum probability solution for the geophysical parameters is finally achieved through the solution of the RTE. The advantage of combining the Tikhonov and the Newtonian methods is to find with objectivity an optimum regularization parameter that is used as a smooth factor to control convergence in the Newtonian retrieval method. In addition, the improved guess parameters obtained from the first-step result in better retrieval performance in the Newtonian retrieval algorithm.

The two-step physical retrieval was applied in this paper to simulated MAS radiances, and a comprehensive error analysis was made. The experimental verification is also presented by application of the algorithm to real MAS observations by a NASA ER-2 aircraft over Oklahoma during the Subsonic Contrails and Clouds Effects Special Studies (SUCCESS) campaign.[22] MAS data is useful for testing the retrieval for MODIS application, because of similarities (cross-track scan pattern, spectral bands, radiometric performance) between MAS and MODIS.[2] Finally the discrepancies between the retrieved parameters and the cross-chain Loran atmospheric sounding system (CLASS) sounding are discussed.

2. Methodology

A. Perturbation Form of the Radiative Transfer Equation

For a cloud-free atmosphere under local thermodynamic equilibrium the RTE[15] in the thermal infrared region may be expressed as

$$R(\nu_j, \mu) = B(\nu_j, t_s)\epsilon(\nu_j, \mu)\tau(\nu_j, \mu, p_s) + R_a(\nu_j, \mu) + \int_0^{2\pi}\int_0^1 \mu' f_r(\mu; -\mu', \phi')R_d(\nu_j, \mu, -\mu', \phi')\mathrm{d}\mu'\mathrm{d}\phi' + \tau^*(\nu_j, \mu, -\mu_0, 0)(-\mu_0)E_0(\nu_j)f_r(\mu; -\mu_0, \phi_0), \quad (1)$$

where $R(\nu_j, \mu)$ is the mean spectral radiance measured in a band whose mean effective wave number is ν_j and the cosine of local zenith angle θ of observation is μ, $B(\nu_j, t_s)$ is the Planck function of the surface skin temperature t_s, $\epsilon(\nu_j, \mu)$ is the effective surface emissivity, and $\tau(\nu_j, \mu, p_s)$ is the transmittance from the surface pressure level p_s to the top of the atmosphere along the observation angle θ. The first term of Eq. (1) represents surface emission to space (less atmospheric absorption). $R_a(\nu_j, \mu)$ is the upwelling radiance contributed from atmosphere to space. $R_d(\nu_j, \mu, -\mu', \phi')$ denotes the atmospheric downwelling emissive radiance being reflected by the surface upward to space; its incident direction is represented by $-\mu'$ and ϕ' (where the minus sign indicates that direction is always downward). Note that $\mu' = \cos\theta'$ and that ϕ' represents the azimuthal angle. The final term represents downward solar radiance reflected off the surface, where μ_0 is the cosine of the solar zenith angle, ϕ_0 is the relative azimuth angle between the viewing direction and the solar beam direction, $f_r(\mu; -\mu', \phi')$ is the bidirectional reflectance distribution function. $\tau^*(\nu_j, \mu, -\mu_0, 0)$, defined as $\tau(\nu_j, \mu, p_s)\tau(\nu_j, -\mu_0, p_s)$, is the total transmittance for the solar beam. $E_0(\nu_j)$ is the spectral solar irradiance incident on the top of the atmosphere (norm to the beam). To be practical with use of Eq. (1) for geophysical parameter retrieval, the following realistic assumptions are held: (a) A horizontally homogeneous atmospheric condition is assumed so that the atmospheric downward thermal emission is independent of azimuth angle.[23] (b) A specular reflection model is adopted, so it is reasonable to assume that $\mu = \mu'$; consequently, the integral of $R_d(\nu_j, \mu, -\mu', \phi')$ can be simplified. (c) A single bidirectional reflectance distribution function anisotropic factor[15] can be used for the surface-reflected solar beam within the shortwave region, and the anisotropic factor α is defined as follows,

$$\alpha = \frac{\pi f_r(\mu; -\mu_0, \phi_0)}{r},$$

where r is reflectance of the assumed Lambertian surface. As a result of above-mentioned assumptions with the relation $r = 1 - \epsilon$ according to Kirchhoff's law, Eq. (1) can be simplified as follows,

$$R(\nu_j, \mu) = B(\nu_j, t_s)\epsilon(\nu_j, \mu)\tau(\nu_j, \mu, p_s) - \int_0^{p_s}\left\{B[\nu_j, t(p)]\frac{\partial\tau(\nu_j, \mu, p)}{\partial p}\right\}\mathrm{d}p + [1 - \epsilon(\nu_j, \mu)]\int_0^{p_s}\left\{B[\nu_j, t(p)]\frac{\partial\tau^*(\nu_j, \mu, -\mu, p)}{\partial p}\right\}\mathrm{d}p + [1 - \epsilon(\nu_j, \mu)]\alpha\tau^*(\nu_j, \mu, -\mu_0, 0)(-\mu_0)\frac{E_0(\nu_j)}{\pi}, \quad (2)$$

where $\tau^*(\nu_j, \mu, -\mu, p) = \tau(\nu_j, \mu, p_s)\tau(\nu_j, -\mu, p_s)/\tau(\nu_j, \mu, p)$ is the reflected transmittance from surface to the pressure level p. Although there is evidence that surface emissivity varies with viewing angle, spectral and angular emissivity data are very limited.[24] In the following derivation, land surfaces are assumed to be Lambertian, (i.e., surface emissivity is independent of local zenith angle), and the solar contribution term is not included (reflected solar radiance correction for daytime observation within the shortwave region is discussed in Subsection 6.C). Equation (2) may be approximated in the numerical perturbation form of

$$\delta t_B(j) = \delta t_s K^{t_s}(j) + \delta\epsilon(j)K^{\epsilon}(j) + \sum_{i=1}^{ls}\delta t(i)K^t(i, j) + \sum_{i=1}^{ls}\{\delta\ln[q(i)]\}K^q(i, j), \quad (3)$$

The sounding retrieval problem has been reduced to one of solving for 11 unknowns (5 temperature eigenvector coefficients, 3 water-vapor eigenvector coefficients, surface skin temperature perturbation plus 2 surface emissivity perturbations).

C. Tikhonov Regularization

The ill-posed problem and the solution of Eq. (4) has been investigated by many in the literature.[28–34] The direct inverse of Eq. (4) may not exist; i.e., there is no solution, or the solution is unstable. Tikhonov regularization[28–31] is the most widely used algorithm to stabilize the ill-posed problem and to obtain a meaningful solution. In our case Tikhonov regulation involves solving the following problem:

$$\underset{\delta f}{\mathrm{Min}}\ \{\|\tilde{K}\delta f - \delta\tilde{y}\|^2 + \gamma^2\|L\delta f\|^2\}, \tag{13}$$

where $\tilde{K} = S^{-1/2}\hat{K}$, $\delta\tilde{y} = S^{-1/2}\delta y$, and $S^{-1/2}$ is the inverse of the root of MAS instrument noise matrix. The symbol γ is a regularization parameter, and L is a side constraint matrix. The solution of Eq. (13) is given by

$$\delta f_\gamma = \tilde{K}_\gamma^{\#}\delta\tilde{y}, \tag{14}$$

where $\tilde{K}_\gamma^{\#}$ is a resolution matrix,

$$\tilde{K}_\gamma^{\#} = (\tilde{K}^T\tilde{K} + \gamma^2 L^T L)^{-1}\tilde{K}^T. \tag{15}$$

The subscript γ indicates that the retrieved expansion coefficients are dependent on γ; different γ results in different solutions. So the regularization parameter γ plays an important role in the retrieved solution. It balances the residual norm $\|\tilde{K}\delta f - \delta\tilde{y}\|$ and the side constraint norm $\|L\delta f\|$. If γ is chosen too small, the solution of Eq. (13) is unstable; whereas if γ is too large, the retrieved solution is close to the initial guess profile. It is possible to find an optimum parameter γ that minimizes the total error. The objective methods that estimate the optimum γ can be found in Refs. 35–37.

D. Newtonian Iteration Algorithm

After the regularization solution described in Subsection 2.C, which updates the original regression guess profile along with the optimum parameter γ, is obtained, the nonlinear Newtonian iteration algorithm is further applied to the Tikhonov regularization solution. The iterative solution of Eq. (4) is given by[17]

$$f_{n+1} = (\tilde{K}_n^T\tilde{K}_n + \gamma_n I)^{-1}[\tilde{K}_n^T(\delta\tilde{y}_n^m + \tilde{K}_n f_n)], \tag{16}$$

where γ_n is a smoothing parameter whose initial value is set to be the output of the Tikhonov regularization algorithm. At each iterative step, convergence tests are carried out. The convergence tests include the expansion coefficient convergence test and the weighted brightness temperature residual test. The purpose of the convergence tests is for retrieval quality control. If one of these tests fails, then the retrieval is rejected. This occurs in less than 0.5% of the retrievals.

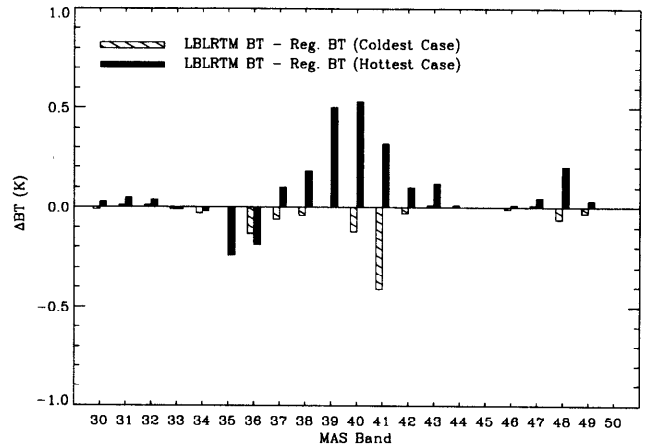

Fig. 3. MAS band synthetic brightness temperature (BT) differences between LBLRTM and fast regression transmittance models (the BT difference is zero if the column is not shown).

3. Forward Transmittance Model

An essential part of the physical retrieval is the accuracy of a fast regression transmittance model for the forward transfer radiance calculation.[38] Following the pressure layer optical depth algorithm,[39] developed for AIRS flying on the EOS PM platform (the satellite will fly in a Sun-synchronous polar orbit ascending northward across the equator in the afternoon), a new MAS fast transmittance regression model has been developed for the current study at Cooperative Institute for Meteorological Satellite Studies (CIMSS). This transmittance model is similar to that used for the high-resolution infrared sounder (HIRS/3) and the advanced microwave sounder unit (AMSU).[40,41] Figure 3 shows brightness temperature differences between LBLRTM and fast regression forward models for MAS bands 30–50. The hottest and coldest rawinsonde observation (RAOB) profiles from a 1-yr RAOB dataset over North America are shown. As seen in Fig. 3, the differences are small (<0.2 K) for all MAS bands except band 41 for the coldest case and bands 39–41 for the hottest case. The largest discrepancy is 0.53 K for band 40, suggesting that the fast regression transmittance model overestimates atmospheric absorption. In Fig. 4, showing results for driest and wettest RAOB profiles, brightness temperature differences for MAS bands 30–50 are less than 0.2 K. This illustrates that the fast regression model has a good agreement with LBLRTM and is able to reproduce line-by-line calculations. One can expect that brightness temperature differences for MAS bands 30–50 from the two models are typically less than 0.2 K, which is near or below nominal MAS noise-equivalent temperature difference (NEΔT).

4. Band Sensitivity Study

A physical algorithm for retrieving geophysical parameters is based on the differences of observed and calculated sounding band brightness temperature.

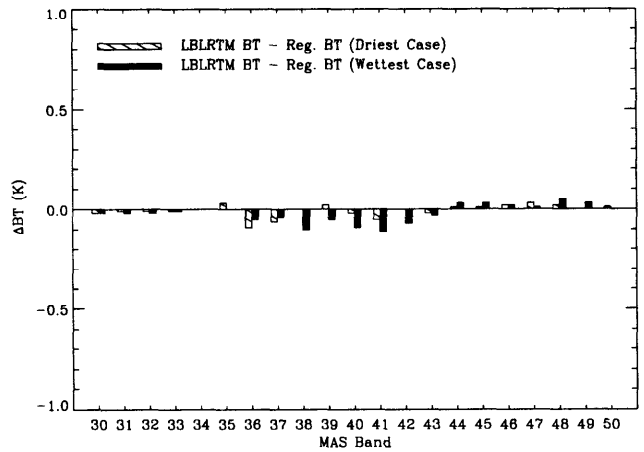

Fig. 4. Same as Fig. 3, but for driest and wettest profiles (the BT difference is zero if the column is not shown).

The brightness temperature differences of MAS bands 30–50 are used in the retrieval. Hence it is important to investigate the MAS bands' sensitivity to variations of the geophysical parameters. The upper panel of Fig. 5 shows the MAS sensitivities to atmospheric temperature variations. The solid and the striped columns show brightness temperature change with addition of 2 and 4 K, respectively, to the hottest temperature profile used in Fig. 3. CO_2 absorption is important ~4.3 μm (MAS bands 34–36) and at wavelengths greater than ~13 μm (MAS bands 48–50).[2] Figure 5 shows that bands 34–36 and 45–50 are the most sensitive bands to

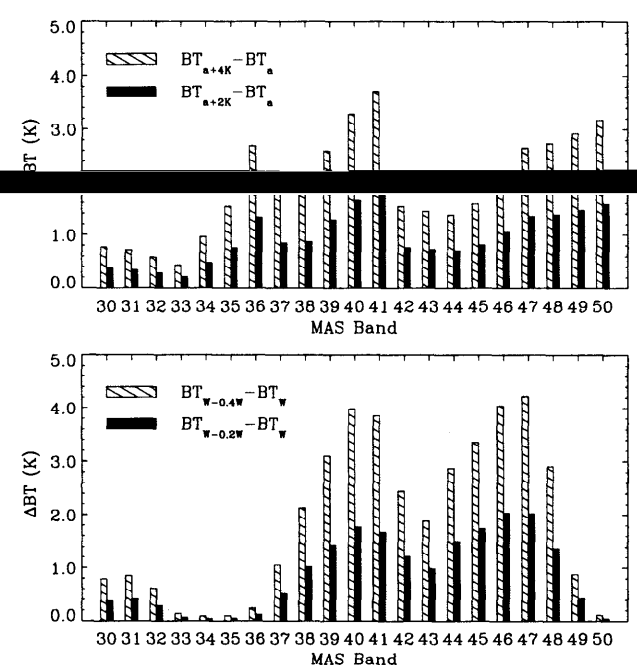

Fig. 5. MAS band brightness temperature difference sensitivity to temperature (top panel) and water-vapor mixing ratio profile (bottom panel) variations. Hottest and wettest profiles of Figs. 3 and 4 are used.

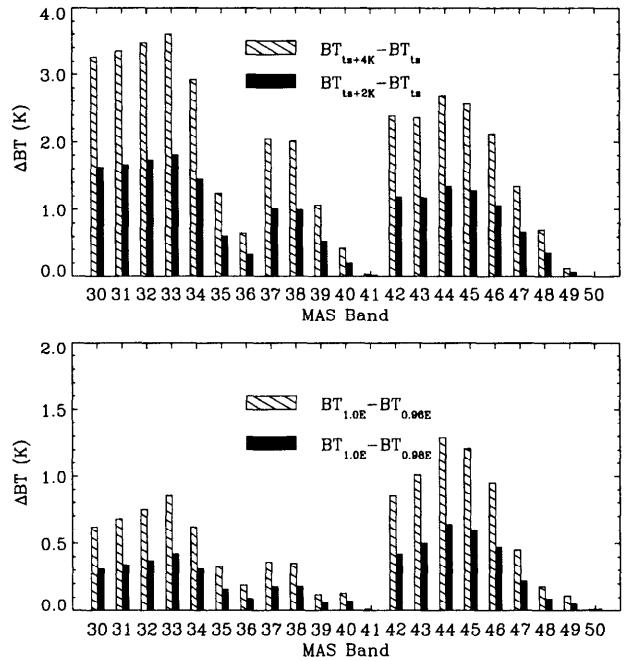

Fig. 6. Same as Fig. 5, but to surface emissivity (top panel) and skin temperature (bottom panel) variations [the brightness temperature (BT) difference is zero if the column is not shown].

atmospheric temperature variation. MAS water-vapor bands 40–42 also are sensitive to temperature variation. This illustrates the strong dependence of water-vapor band radiance on atmospheric temperature. The solid and the striped columns in the bottom panel of Fig. 5 are with 20% and 40% water-vapor mixing ratio reduction, respectively, from the wettest profile of Fig. 4. As can be seen, bands 38–42 and 44–47 are sensitive to atmospheric water-vapor changes. MAS band 48, which is used mainly for temperature retrieval, also has large sensitivity to atmospheric water vapor. It is demonstrated that all geophysical parameters being retrieved make sensitive contributions to the brightness temperature of sounding bands. Thus a simultaneous retrieval approach may perform better than a sequential retrieval approach (geophysical parameters are retrieved separately), because the interdependence of atmospheric status with the coupled surface contribution is taken into account.

Figure 6 shows MAS sensitivity to surface skin temperature and emissivity variations from the hottest temperature profile used in Fig. 3. The original surface emissivity is assumed to be 1.0 (blackbody). Emissivity changes of 0.02 and 0.04 are shown. The changes of surface skin temperature are 2 and 4 K, respectively. It can be seen that bands 30–34 and 42–46 (except ozone band 43) are the most sensitive to the change of surface properties. These spectral bands enable study of surface properties. In summary, the sensitivity study of the MAS bands demonstrates that, although MAS is not a sounder instrument, it does have many thermal infrared

Table 2. List of Terrestrial Material Samples[a]

Sample No.	Sample Name	Type of Material
1	basalt.f	Fresh rough surface
2	basalt.v	Desert vanish coated rock
3	ijolite.f	Fresh rough surface
4	ijolite.v	Desert vanish coated rock
5	rhyolite.f	Fresh rough surface
6	rhyolite.v	Desert vanish coated rock
7	crustose.10	Lichens coated rock
8	crustose.65	Lichens coated rock
9	basalt.h7	Igneous rock
10	dunite.h1	Igneous rock
11	granite.h1	Igneous rock
12	syenite.h1	Igneous rock
13	greywack.eh1	Sedimentary rock
14	limeston.eh1	Sedimentary rock
15	limeston.eh2	Sedimentary rock
16	limeston.eh3	Sedimentary rock
17	sandton.eh1	Sedimentary rock
18	sandton.eh2	Sedimentary rock
19	sandton.eh4	Sedimentary rock
20	shale.h3	Sedimentary rock
21	shale.h5	Sedimentary rock
22	shale.h6	Sedimentary rock
23	siltton.eh1	Sedimentary rock
24	siltton.eh2	Sedimentary rock
25	gneiss.h1a	Metamorphic rock
26	gneiss.h3a	Metamorphic rock
27	gneiss.h4	Metamorphic rock
28	marble.h2	Metamorphic rock
29	marble.h3	Metamorphic rock
30	marble.h4	Metamorphic rock
31	quartzit.eh1	Metamorphic rock
32	quartzit.eh4	Metamorphic rock
33	quartzit.eh6	Metamorphic rock
34	schist.h3a	Metamorphic rock
35	schist.h6a	Metamorphic rock
36	schist.h7	Metamorphic rock
37	slate.h1a	Metamorphic rock
38	slate.h2a	Metamorphic rock
39	slate.h3	Metamorphic rock
40	0127	Soil (Spodosols)
41	0135	Soil (Entisols)
42	0145	Soil (Ultisols)
43	0211	Soil (Molisols)
44	0219	Soil (Alfisols)
45	0226	Soil (Inceptisols)
46	0475	Soil (Vertisols)
47	1530	Soil (Aridisols)
48	4717	Soil (Oxisols)
49	foliose.1	Veg., lichens
50	indiangr.ass	Veg., green foliage
51	redoak	Veg., green foliage
52	white.ine	Veg., green foliage
53	senbeech	Veg., senescent foliage
54	senpine	Veg., senescent foliage
55	senredoa.kh1	Veg., senescent foliage
56	senryegr.ass	Veg., senescent foliage
57	oakbark.1	Veg., tree bark
58	pinebark.1	Veg., tree bark
59	ypoplarb.ark	Veg. senescent foliage
60	conifer.ous	Veg. decomposing litter
61	decidu.ous	Veg. decomposing litter
62	wood	Veg. decomposing litter
63	seawater	Water
64	distwa.ter	Water
65	distice.00g	Ice
66	distices.moo	Ice
67	seaice.10.ogr	Ice
68	seaicesm.oot	Ice
69	qtzwater.23	Suspended sediments
70	qtzwater.64	Suspended sediments
71	qtzwater.7	Suspended sediments
72	foam	Water coatings
73	oil15465	Water coatings
74	oil34792	Water coatings
75	oil39076	Water coatings
76	oil42667	Water coatings
77	soilfl.oat	Water coatings
78	qtzfloat	Water coatings
79	oil35473	Water coatings
80	qtz.hem	Quartz

[a]Ref. 15.

bands that contain information to be used for retrieving geophysical parameters.

5. Band-Averaged Land-Surface Emissivity

The band-averaged land-surface emissivity is defined as

$$\epsilon(j) = \frac{\int_{\nu_{j,l}}^{\nu_{j,u}} \psi(\nu)\epsilon(\nu)\mathrm{d}\nu}{\int_{\nu_{j,l}}^{\nu_{j,u}} \psi(\nu)\mathrm{d}\nu}, \tag{17}$$

where $\psi(\nu)$ is the spectral response function of the MAS band j, and $\nu_{j,l}$ and $\nu_{j,u}$ are its lower and upper spectral boundaries. MAS band-averaged emissivity data were calculated with Eq. (17) from published spectral reflectance data of 80 pure terrestrial material samples. These material samples include igneous, metamorphic, and sedimentary rocks, varnished rock surface, lichen-covered sandstone, soil samples, green foliage, senescent foliage, water, ice, and water surfaces with suspended quartz sediment or oil slicks. The sample numbers, names, and corresponding type of material are summarized in Table 2. A more detailed description of these surface emissivity data can be found in Refs. 42 and 43. Figure 7 shows the calculated band-averaged surface emissivities in the MAS bands 30–32, 42, 45, 46, and 48. Analysis of these emissivity data clearly shows that there are strong variations not only for different terrestrial materials (from vegetated surfaces to rock and sand) at given spectral positions but also for given materials at different spectral regions. For simplicity, in the two-step physical retrieval algorithm tested in this paper, only two surface emissivities are retrieved. These two emissivities are

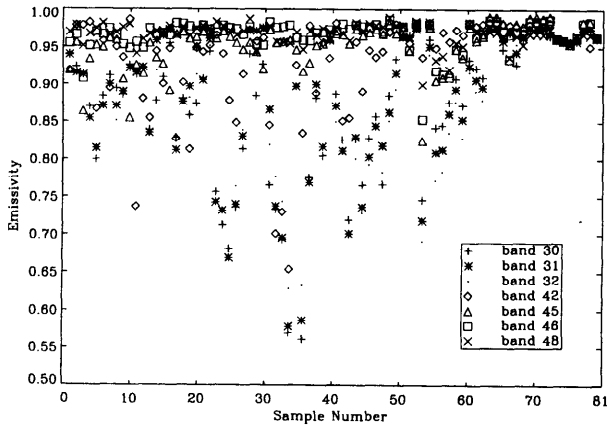

Fig. 7. Band-averaged emissivities of 80 terrestrial material samples in MAS bands 30–32, 42, 45, 46, and 48.

band-averaged emissivities for MAS shortwave (3–5-μm) and longwave (8–14.5-μm) regions.

6. Retrieval Results

The two-step physical retrieval algorithm was tested with both simulated MAS radiances (from radiosondes) and real MAS observations over Oklahoma during the SUCCESS campaign. For generating a first-guess profile, a regression-based retrieval was performed on the MAS datasets. The data components and the retrieval results are described in this section.

A. First-Guess Regression Retrieval

To develop a first-guess regression retrieval, 2512 radiosonde profiles from the period of 2 March to 11 April 1996 over the central United States were used. The radiosondes were divided into dependent (2094 profiles) and independent (418 profiles) datasets. An eigenvector decomposition technique was applied to the dependent dataset to describe the temperature and water-vapor mixing ratio profiles. Two sets of empirical orthogonal functions were calculated; one for temperature and one for the natural logarithm of water-vapor mixing ratio. As described in Subsection 2.B, each atmospheric profile can be expanded in terms of a few empirical orthogonal functions to capture the atmospheric vertical structure information. The surface skin temperature was simulated for each radiosonde from surface air temperature plus a random number with variance 4 K and mean value equal to zero. The shortwave and the longwave surface emissivities used in forward calculations were the MAS band-averaged emissivity data described in Section 5. The surface emissivities vary from 0.56 to 0.99.

The forward model discussed in Section 3 was used to create MAS simulated brightness temperatures for each radiosonde profile in the dependent and the independent datasets. Random noise based on actual MAS data (variance 0.2 K and mean value equal to zero) was added to the MAS simulated dataset for better simulation of the MAS real observations.

Regression analysis was applied to the dependent radiosonde-simulated MAS dataset to generate regression coefficients relating MAS bands 30–50 to atmospheric temperature and water-vapor profiles, surface skin temperature, and shortwave and longwave emissivities. The regression coefficients were applied to the independent dataset to produce a high-quality profile of atmospheric state and surface properties to facilitate physical solution of the RTE. Temperature and water-vapor profile statistical comparisons are given in Fig. 8. The solid and the dashed curves represent the root-mean-square (rms) errors for physical (discussed in Subsection 6.B) and regression retrievals, respectively. The corresponding rms error (dotted–dashed curve) of the dependent mean profile is also plotted. As shown, the regression retrieval first guess is a large improvement over the mean profile for both temperature and water vapor.

B. Two-Step Physical Retrieval Test

The two-step physical retrieval algorithm described in Section 2 is performed as follows: In the first step the Tikhonov regularization parameter is determined and applied to the first guess profile from the regression analysis. The constraint matrix L is simply set to satisfy $L^T L = C^{-1}$, where C is a matrix of geophysical parameter expected errors as its entries. The MAS instrument noise was evaluated with data collected over the Gulf of Mexico on 9 April 1996. A set of the expansion coefficients from Eq. (14) is computed as a Tikhonov parameter γ varies. Then the Tikhonov solution that updates the first-guess profile is obtained. The retrieved residual of the MAS bands 30–50 is estimated at each step. The residual is defined to be the rms error of the noise-weighted difference between the observed brightness temperature and the brightness temperature calculated from the retrieved geophysical parameters through the RTE. This procedure is repeated with a varied γ. When the retrieved residual is minimized, the first step is completed. The Tikohonov parameter γ from the first step is referred to as the optimum parameter in the sense of minimizing the retrieved residual. If the minimum of retrieved residual is greater than the guess residual calculated from the regression analysis, the Tikhonov solution is rejected, and the first step retrieval is replaced with the regression profile with the optimum parameter set to an empirical value.

In the second step, following the same procedure as in Ref. 17, the nonlinear Newtonian iteration algorithm is applied to the updated first-guess profile to produce the final two-step physical retrieval. Table 3 lists the rms errors of the retrieval comparisons for a zero noise case. The second column represents the rms departure of the independent dataset profiles from the mean profile of the dependent dataset. The third and the forth columns are rms errors of the regression and two-step physical retrieved results compared with the MAS simulated data from the independent dataset profiles. The layer mean tem-

Table 3. Retrieval rms of Independent Dataset Simulated for 418 Profiles, with no Noise Added

	Dep. Mean Profile	Regression Rtvl.	Physical Rtvl.
Layer (hPa)[a]	T (K)	T (K)	T (K)
1 (50–200)	4.46	1.04	0.89
2 (200–400)	3.32	1.49	1.42
3 (400–600)	5.62	1.26	1.14
4 (600–800)	6.96	1.25	1.18
5 (800–1000)	8.23	1.84	1.64
Ts (K)	10.59	0.62	0.49
TPW (cm)	0.85	0.49	0.34
Sw ϵ	0.060	0.024	0.020
Lw ϵ	0.0279	0.012	0.009

[a]Ts, surface skin temperature; TPW, total precipitable water vapor; Sw ϵ, surface emissivity in the shortwave region; Lw ϵ, surface emissivity in the longwave region.

Table 4. Retrieval RMS of Independent Dataset Simulated for 418 Profiles, Noise (mean = 0 and std = 0.2 K) Added

	Dep. Mean Profile	Regression Rtvl.	Physical Rtvl.
Layer (hPa)[a]	T (K)	T (K)	T (K)
1 (50–200)	4.46	1.04	0.99
2 (200–400)	3.32	1.49	1.48
3 (400–600)	5.62	1.26	1.21
4 (600–800)	6.96	1.25	1.18
5 (800–1000)	8.23	1.84	1.73
Ts (K)	10.59	0.62	0.58
TPW (cm)	0.85	0.49	0.38
Sw ϵ	0.060	0.024	0.022
Lw ϵ	0.029	0.012	0.011

[a]Ts, surface skin temperature; TPW, total precipitable water vapor; Sw ϵ, surface emissivity in the shortwave region; Lw ϵ, surface emissivity in the longwave region.

perature (LMT) 1 is the temperature profile averaged from 50 to 200 hPa. The other LMT's are averaged from 200–400, 400–600, 600–800, and 800–1000 hPa. The rms departure of the LMT from the dependent mean profile is from 4.46–8.23 K, whereas the rms error of the two-step physical retrieval is 1.64 K or less. The total precipitable water vapor (TPW) rms is dramatically reduced from 0.85 to 0.34 cm. For surface properties the rms error of skin temperature is 0.49 K, and the rms error of surface emissivity is 0.020 (0.009) for the shortwave (longwave) region. Figure 8 displays the information of Table 3 in graphical form. Table 4 lists the same statistical comparisons as Table 3 but with random noise 0.2 K added into the simulated data. For a random NEΔT of 0.2 K, the statistical results show that rms errors for LMT and TPW retrievals are equal to or less than 1.73 K and 0.38 cm, respectively. The rms error of surface skin temperature is 0.58 K. And surface emissivity retrieval errors within the shortwave and the longwave regions are 0.022 and 0.011, respectively. Obviously, as noise increases the accuracy of the retrieval is degraded but still quite good. For noise of 0.2 K the rms error of the TPW is still ~22% less than the regression retrieval results (0.38 cm versus 0.49 cm). Improvements of surface properties are mitigated as noise increases. However, in Table 4 the physical retrieval rms error of the LMT and the surface emissivities is slightly better than the regression retrieval rms error. In summary statistical analysis of retrieval rms errors show that the two-step physical retrieval algorithm is able to retrieve geophysical parameters simultaneously with improved accuracy by use of MAS simulated data.

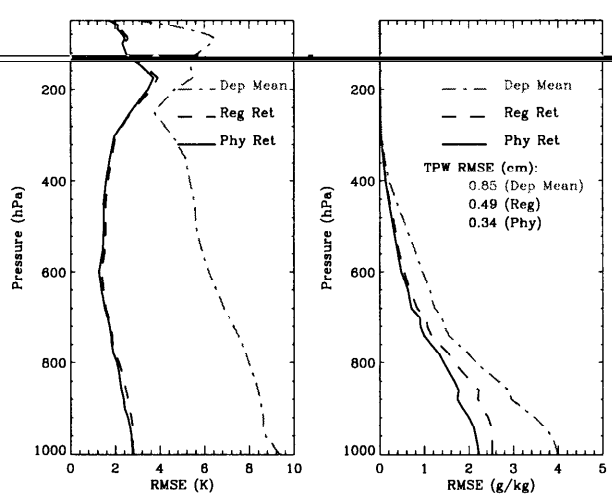

Fig. 8. Retrieved rms errors of temperature and water-vapor mixing ratio from the MAS synthetic brightness temperatures.

C. Retrieval with Real MODIS Airborne Simulator Data

The two-step physical retrieval algorithm described in Section 2 was applied to real MAS multispectral measurements from the SUCCESS campaign. Clear-sky radiances on 13 April 1996 were collected from 18:26 to 18:34 UTC by MAS on a NASA ER-2 aircraft over the Cloud and Radiation Testbed site in Oklahoma. The MAS 50-m-resolution image contained 2991 lines with 716 pixels per line. The MAS data were averaged to a 10 × 10 field-of-view clear brightness temperature vector for each retrieval. The averaging process reduced the image size to 70 pixels per line by 300 lines. The MAS 3–5 μm band radiances were adjusted to remove surface-reflected solar contamination.[44,45] For better representation of surface type in Oklahoma, some material samples such as minerals and rocks were excluded from the MAS band-averaged surface emissivity data in Section 5. A newly averaged two-emissivity dataset within the shortwave and the longwave regions was generated, which is a subset of MAS band-averaged emissivity data. This was randomly incorporated into the dependent and the independent datasets for the MAS simulated brightness temperature calculation. A new set of regression coefficients that relate the geophysical parameters to the MAS simulated brightness temperature was generated from the dependent dataset. Surface pressure and sensor viewing angle were added as additional predictors along with MAS band measurements, since surface pres-

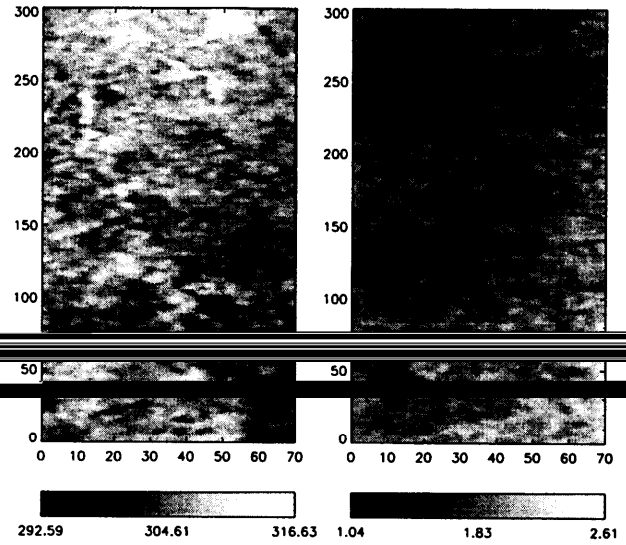

Fig. 9. Surface skin temperature (in kelvins) and total precipitable water-vapor (in centimeters) images retrieved from the MAS real observations.

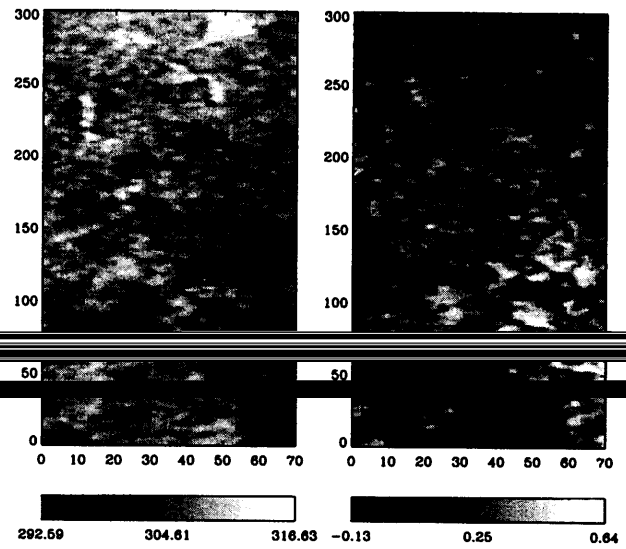

Fig. 11. Relationship between retrieved surface skin temperature and normalized difference vegetation index.

sure and sensor viewing angle variations must be accounted for in the real observations. Figure 9 shows the retrieved surface skin temperature (left-hand panel) and total precipitable water-vapor (right-hand panel) images, respectively, from the two-step physical algorithm. The range of retrieved surface skin temperature is 292.6–316.6 K. The retrieved TPW range is 1.04–2.61 cm. The retrieved surface emissivities within the shortwave and the longwave regions are given in Fig. 10. The surface emissivity variation is from 0.93–1.00. For the indirect verification of surface skin temperature the normalized difference vegetation index (NDVI) is displayed in the right-hand panel of Fig. 11. The NDVI was determined on the basis of the relationship between measurements of MAS reflectance bands 2 (0.66 μm) and 7 (0.87 μm):

$$\mathrm{NDVI} = \frac{\mathrm{ref}(7) - \mathrm{ref}(2)}{\mathrm{ref}(7) + \mathrm{ref}(2)}, \tag{18}$$

where ref(7) and ref(2) are reflectances of visible bands 7 and 2, respectively. The NDVI approximately describes terrestrial material status: The higher NDVI value indicates vegetation, whereas lower NDVI values are typically nonvegetated surface.[46,47] As shown in Fig. 11, skin temperature is inversely correlated to NDVI, and higher (lower) skin temperature (left-hand panel) corresponds to lower (higher) NDVI.[13] Figure 12 shows the correlation between surface skin temperature and the NDVI. The calculated correlation coefficient is −0.75 with 21,229 retrieval points. It can be seen that there is a good negative correlation between the NDVI and retrieved surface skin temperature. A collocated

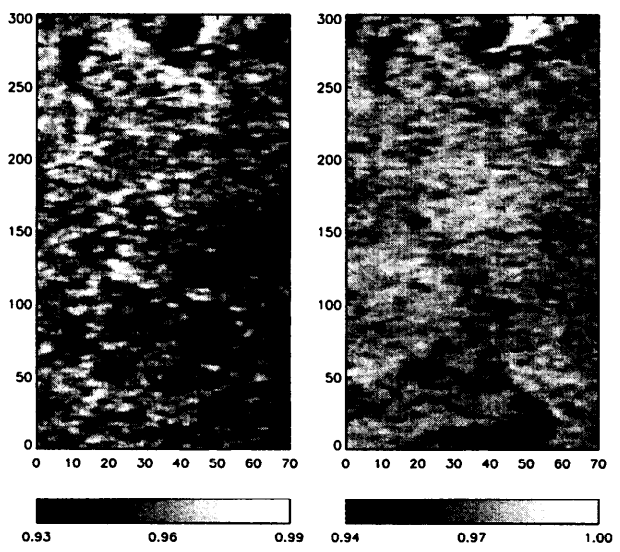

Fig. 10. Same as Fig. 9, but for retrieved surface emissivities within the shortwave and the longwave regions.

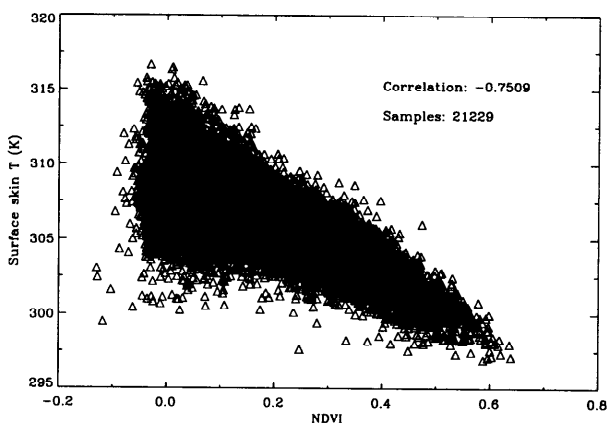

Fig. 12. Scatter diagram of retrieved surface skin temperature versus NDVI.

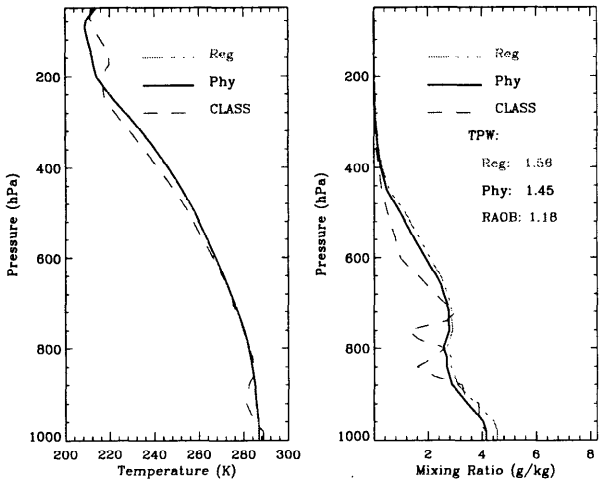

Fig. 13. Temperature and water-vapor mixing ratio retrieval comparisons with CLASS sounding profile at Cloud and Radiation Testbed site.

CLASS sounding profile at 18 UTC was selected for atmospheric parameter comparison. The nearest (5 km) retrieved profile to the CLASS profile was chosen. The observation time difference was approximately 30 min. Figure 13 illustrates the comparison of temperature and water-vapor mixing ratio profiles. The dashed curve is the CLASS sounding profile and the solid and the dotted–dashed curves represent physical and regression solutions, respectively. Although the physical retrieval is not an improvement over the regression temperature profile, the retrieval of the water-vapor mixing ratio profile from the two-step algorithm agrees better with the CLASS sounding than does the regression profile. The TPW bias error is reduced by ~9% (1.45 versus 1.56). The discrepancies between the CLASS sounding and retrieved profiles occur for the following reasons: (a) the MAS instrument with the lower vertical resolution capability has difficulty capturing sharp vertical gradients in the geophysical parameters, (b) the spatial resolution of the measurements differs (point measurement versus area average), (c) temporal discrepancies between the measurements (CLASS at 18:00 UTC, MAS at 18:26–18:34 UTC), (d) the CLASS sounding errors are of the order of 0.5 K for temperature and 10% for humidity,[48–50] and (e) there is no bias correction to MAS radiances. Bias corrections account for absolute instrument measurement error, forward model error, and other processing errors. In addition, the current two-step physical retrieval algorithm is limited to retrieve only two surface emissivities (one within the shortwave region, the other within the long-wave region). They may not represent real emissivity spectral variation, especially in the shortwave region when nonvegetated surfaces are viewed. However it is possible to retrieve more than two surface emissivities if the reflected solar contribution term in Eq. (1) is included in the perturbation form of the RTE. This term is related to the surface properties and atmospheric conditions in the lower troposphere. Thus it includes information that can improve the accuracy of atmospheric parameter and surface property retrievals. Currently this investigation is under way. Preliminary testing shows that the retrieval accuracy of surface emissivities, especially within the shortwave region, is significantly improved when the reflected solar contribution term is included in Eq. (1). The test results will be presented in a future paper.

7. Conclusion

In this paper we have presented a two-step physical algorithm for simultaneous retrieval of geophysical parameters including atmospheric temperature and water-vapor profiles, surface skin temperature, and shortwave and longwave emissivity from MAS radiometric measurements. Previously, it was assumed that the surface is a blackbody or graybody for atmospheric sounding or that atmospheric properties are well known for surface property retrieval. As demonstrated in Ref. 13, the assumption of fixed surface emissivity degrades the accuracy of atmospheric parameter retrieval in the troposphere. The advantage of the two-step physical algorithm presented here is to retrieve atmospheric parameters along with surface properties simultaneously in the coupled Earth–atmosphere system. Retrievals of geophysical parameters with MAS simulated brightness temperatures calculated for a radiosonde profile dataset show that the accuracy of all retrieved parameters is improved as compared with regression retrieval. When random noise of 0.2 K is added into the simulated data, retrieval performance is degraded. However, RMS statistics demonstrate that the results retrieved with the two-step physical algorithm are still better than regression retrieval results. The rms error (Table 4) of retrieved layer mean temperature is equal to or less than 1.73 K; the rms error of total precipitable water is 0.38 cm, a 22% reduction of rms as compared with rms of the regression retrieval. Surface property (skin temperature, emissivity) retrieval is also improved. rms's of 0.58 K and 0.022 (0.011) are achieved for retrieved surface skin temperature and shortwave (longwave) emissivities, respectively. The experimental verification was also extended to real MAS observations from a NASA ER-2 aircraft over Oklahoma during the SUCCESS campaign. The retrieved temperature and water-vapor mixing ratio profiles compared well with a CLASS sounding. The TPW retrieved from the two-step physical algorithm is 1.45 cm, 9% better than regression retrieval results. Surface properties were indirectly verified with NDVI computed from MAS data. A high negative correlation (−0.75) was found between retrieved skin temperature and NDVI.

We are indebted to H. M. Woolf for his dedicated contributions to the MAS transmittance model development and providing all RAOB data used in this

study. Our sincere appreciation is also extended to H. L. Huang and J. Li for valuable discussion on the algorithm development and to Y. Plokhenko for providing the MAS dataset. This research was supported by EOS program contracts NA55-31370 and NA55-31367 of NASA.

References and Note

1. V. V. Salomonson, W. L. Barnes, P. W. Maymon, H. E. Montgomery and H. Ostrow, "MODIS: advanced facility instrument for studies of the Earth as a system," IEEE Trans. Geosci. Remote Sens. **27,** 145–153 (1998).
2. M. D. King, W. P. Menzel, P. S. Grant, J. S. Myers, G. T. Arnold, S. E. Platnick, L. E. Gumley, S. C. Tsay, C. C. Moeller, M. Fitzgerald, K. S. Brown, and F. G. Osterwisch, "Airborne scanning spectrometer for remote sensing of cloud, aerosol, water vapor, and surface properties," J. Atmos. Ocean. Technol. **13,** 777–794 (1996).
3. W. P. Menzel and L. E. Gumley, "MODIS atmospheric profile retrieval algorithm theoretical basis document," (Earth Observing System Project Science Office, NASA Goddard Space Flight Center, Greenbelt, Md., 1998).
4. S. A. Clough and M. J. Iacono, "Line-by-line calculations of atmospheric fluxes and cooling rates. 2. Applications to carbon dioxide, ozone, methane, nitrous oxide and the halocarbons," J. Geophys. Res. **100,** 16519–16535 (1995).
5. W. L. Smith, H. M. Woolf, and A. J. Schriener, "Simultaneous retrieval of surface and atmospheric parameters: a physical and analytically direct approach," in *Advances in Remote Sensing Retrieval Method*, A. Deepak, H. E. Flemming, and M. T. Chahine, eds. (Deepak, Hampton, Va., 1985), pp. 221–232.
6. W. L. Smith, H. M. Woolf, H. B. Howell, H.-L. Huang, and H. E. Revercomb, "The simultaneous retrieval of atmospheric temperature and water vapor profiles—application to measurements with the high spectral resolution interferometer sounder (HIS)," in *Advances in Remote Sensing Retrieval Methods*, A. Deepak, H. E. Flemming, and J. S. Theon, eds. (Deepak, Hampton, Va., 1989), pp. 189–202.
7. W. L. Smith, H. E. Revercomb, H. B. Howell, H.-L. Huang, R. O. Knuteson, E. W. Koenig, D. D. LaPorte, S. Silverman, L. A. Sromovsky, and H. M. Woolf, "GHIS—the GOES high-resolution interferometer sounder," J. Appl. Meteorol. **29,** 1189–1204 (1990).
8. W. L. Smith, H. M. Woolf, and H. E. Revercomb, "Linear simultaneous solution for temperature and observing constituent profiles from radiance spectra," Appl. Opt. **30,** 1117–1123 (1991).
9. W. L. Smith, H. M. Woolf, C. M. Hayden, and A. J. Schreiner, "The simultaneous retrieval export package," presented at the Second International TOVS Study Conference, Igls, Austria, 18–22 February 1985 (Cooperative Institute for Meteorological Satellite Studies, University of Wisconsin—Madison, Madison, Wis., 1985), pp. 224–253.
10. H.-L. Huang, "An analysis of the characteristics of the atmospheric profiles obtained with the High-Resolution Interferometer Sounder (HIS)," Ph.D. dissertation (University of Wisconsin—Madison, Madison, Wis., 1989).
11. C. H. Hayden, "GOES-VAS simultaneous temperature-moisture retrieval algorithm," J. Appl. Meteorol. **27,** 705–733 (1988).
12. T. Schmidt, National Oceanic and Atmospheric Administration/National Environmental Satellite, Data, and Information Service, Office of Research and Applications, Advanced Satellite Products Team, Madison, Wis. 53706 (personal communication, 2000).
13. Y. Plokhenko and W. P. Menzel, "The effects of surface reflection on estimating the vertical temperature–humidity distribution from spectral infrared measurements," J. Appl. Meteorol. **39,** 3–14 (2000).
14. Z. M. Wan and J. Dozier, "A generalized split-window algorithm for retrieving land-surface temperature from space," IEEE Trans. Geosci. Remote Sens. **34,** 892–905 (1996).
15. Z. M. Wan and Z. L. Li, "A physics-based algorithm for retrieving land-surface emissivity and temperature from EOS/MODIS data," IEEE Trans. Geosci. Remote Sens. **35,** 980–996 (1997).
16. B. Huang, "New approach to simultaneous retrieval of atmospheric profiles from radiance spectra," Ph.D. dissertation (University of Wisconsin—Madison, Madison, Wis., 1998).
17. X. L. Ma, T. J. Schmit, and W. L. Smith, "A non-linear physical retrieval algorithm—its application to the GOES-8/9 sounder," J. Appl. Meteorol. **38,** 501–513 (1999).
18. J. Li and H. L. Huang, "Retrieval of atmospheric profiles from satellite sounder measurements by use of the discrepancy principle," Appl. Opt. **38,** 916–923 (1999).
19. J. R. Eyre, "Inversion of cloudy satellite sounding radiances by nonlinear optimal estimation. I. Theory and simulation for TOVS," Q. J. R. Meteorol. Soc. **115,** 1001–1026 (1989).
20. J. R. Eyre, "Inversion of cloudy satellite sounding radiances by nonlinear optimal estimation. II. Application to TOVS data," Q. J. R. Meteorol. Soc. **115,** 1027–1037 (1989).
21. W. L. Smith, H. L. Huang, M. S. Whipple, and S. P. Ho, "UW-CIMSS physical retrieval system science document for AIRS/AMSU/MHS," AIRS science team document (Jet Propulsion Laboratory, NASA, Pasedena, Calif., 1996).
22. O. B. Toon and R. C. Miake-Lye, "Subsonic aircraft: contrail and cloud effects special study (SUCCESS)," Geophys. Res. Lett. **25,** 1109–1112 (1998).
23. W. L. Smith, R. O. Knuteson, H. E. Revercomb, W. Feltz, H. B. Howell, W. P. Menzel, N. R. Nalli, O. Brown, J. Brown, P. Minnett, and W. McKeown, "Observations of the infrared radiative properties of the ocean-implications for the measurement of sea surface temperature via satellite remote sensing," Bull. Am. Meteorol. Soc. **77,** 41–51 (1996).
24. W. C. Snyder, Z. M. Wan, Y. L. Zhang, and Y. Z. Feng, "Thermal infrared (3–14 μm) bidirectional reflectance measurements of sands and soils," Remote Sens. Environ. **60,** 101–109 (1997).
25. J. Li, "Temperature and water vapor weighting functions from radiative transfer equation with surface emissivity and solar reflectivity," Adv. Atmos. Sci. **11,** 421–426 (1994).
26. The 40 levels for the MAS aircraft pressure coordinates are as follows: 50, 60, 70, 75, 80, 85, 90, 100, 125, 150, 175, 200, 250, 300, 350, 400, 450, 500, 550, 600, 620, 640, 660, 680, 700, 720, 740, 760, 780, 800, 820, 840, 860, 880, 900, 920, 940, 960, 980, and 1000 hPa.
27. W. L. Smith and H. M. Woolf, "The use of eigenvectors of statistical covariance matrices for interpreting satellite sounding radiometer observations," J. Atmos. Sci. **33,** 1127–1140 (1976).
28. A. N. Tikhonov, "Solution of incorrectly formulated problems and the regularization method," Sov. Math. Dokl. **4,** 1035–1038 (1963).
29. A. N. Tikhonov, "Regularization of incorrectly posed problems," Sov. Math. Dokl. **4,** 1624–1627 (1963).
30. A. N. Tikhonov and V. Y. Arsenin, *Solutions of Ill-Posed Problems* (Winston, Washington, D.C., 1977).
31. A. N. Tikhonov, A. V. Goncharsky, V. V. Stepanov, and A. G. Yagola, *Numerical Methods for the Solution of Ill-Posed Problems* (Kluwer, Dordrecht, the Netherlands, 1995).
32. G. Bachus and F. Gillbert, "Uniqueness in the inversion of inaccurate gross earth data," Philos. Trans. R. Soc. London Ser. A **266,** 123–192 (1970).
33. S. Twomey, "On the numerical solution of Fredholm integral equations of the first kind by the inversion of the linear system

produced by quadrature," J. Assoc. Comput. Math. **10,** 97–101 (1963).
34. C. D. Rodgers, "Retrieval of atmospheric temperature and composition from remote measurements of thermal radiation," Rev. Geophys. Space Phys. **14,** 609–624 (1976).
35. P. C. Hansen, "Rank-deficient and discrete ill-posed problems," Ph.D. dissertation (Technical University of Denmark, Lyngby, Denmark, 1996).
36. G. Wahba, "Ill-posed problems: numerical and statistical methods for mildly, moderately and severely ill-posed problems with noise data," Tech. Rep. **595,** (Statistics Department, University of Wisconsin-Madison, Madison, Wis., 1980).
37. G. Wahba, *Spline Methods for Observational Data*, Vol. 59 of CBMS-NSF Regional Conference Series in Applied Mathematics (Society for Industrial and Applied Mathematics, Philadelphia, Pa., 1990).
38. J. R. Eyre, "A fast radiative transfer model for satellite sounding systems," Tech. Memo **176,** (European Centre for Medium-Range Weather Forecast, Reading, UK, 1991).
39. S. Hannon, L. L. Strow, and W. W. McMillan, "Atmospheric infrared fast transmittance model: a comparison of two approaches," in *Optical Spectroscopic Techniques and Instrumentation for Atmospheric and Space Research II*, P. B. Hays and J. Wang, eds., Proc. SPIE **2830,** 94–105 (1996).
40. H. M. Woolf, P. V. Delst, and W. J. Zhang, "NOAA-15 HIRS/3 and AMSU transmittance model validation," in *Proceedings of the Tenth International TOVS Study* (Bureau of Metrology Resource Center, Melbourne, 1999), pp. 564–573.
son, "Validation of FASCODE3 and MODTRAN3: comparison of model calculations with ground-based and airborne interferometer observations under clear-sky conditions," Appl. Opt. **35,** 6028–6040 (1996).
42. J. W. Salisbury and D. M. D'Aria, "Emissivity of terrestrial materials in the 8–14 μm atmospheric window," Remote Sens. Environ. **42,** 83–106 (1992).
43. J. W. Salisbury and D. M. D'Aria, "Emissivity of terrestrial materials in the 3–5 μm atmospheric window," Remote Sens. Environ. **47,** 345–361 (1994).
44. W. L. Smith, H. M. Woolf, P. G. Abel, C. M. Hayden, M. Chalfant, and N. Grody, "NIMBUS-5 sounder data processing system. Part 1. Measurement characteristics and data reduction procedures," NOAA Tech. Memo NESS **57** (National Oceanic and Atmospheric Administration, Washington, D.C., 1974), pp. 36–41.
45. C. M. Hayden and T. J. Schmit, "Initial evaluation of the GOES-8 sounder," presented at the Ninth Symposium on Meteorological Observations and Instrumentation Charlotte, N.C., 27–31 March 1995 (American Meteorological Society, Boston, Mass., 1995), pp. 385–390.
46. C. J. Tucker, "Red and photographic infrared linear combinations for monitoring vegetation," Remote Sens. Environ. **8,** 127–150 (1979).
47. C. O. Justice, J. R. G. Townshend, B. N. Holben, and C. J. Tucker, "Analysis of the phenology of global vegetation using meteorological satellite data," Int. J. Remote Sens. **6,** 1271–1318 (1985).
48. F. J. Schmidlin, "WMO international radiosonde comparison, phase II," Final Rep. 1985, in *Instruments and Observing Methods,* Rep. 29, WMO/TD 312 (World Meteorological Organisation, Geneva, Switzerland, 1985), pp. 1–113; available from WMO Secretariat, 41 Avenue Giuseppe Motta, Case Pos-
49. C. G. Wade, "An evaluation of problems affecting measurement of low relative humidity on the United States radiosonde," J. Atmos. Ocean. Technol. **11,** 687–700 (1994).
50. R. W. Pratt, "Review of radiosonde humidity and temperature errors," J. Atmos. Ocean. Technol. **2,** 404–407 (1985).